

Microscopically based energy density functionals for nuclei using the density matrix expansion: Implementation and pre-optimization

M. Stoitsov,^{1,*} M. Kortelainen,^{1,†} S. K. Bogner,^{2,3,‡} T. Duguet,^{2,3,4,§} R. J. Furnstahl,^{5,||}
B. Gebremariam,^{2,3,¶} and N. Schunck^{1,**}

¹*Department of Physics & Astronomy, University of Tennessee, Knoxville, Tennessee 37996, USA and
Physics Division, Oak Ridge National Laboratory, Oak Ridge, Tennessee 37831, USA*

²*National Superconducting Cyclotron Laboratory, 1 Cyclotron Laboratory, East Lansing, Michigan 48824, USA*

³*Department of Physics and Astronomy, Michigan State University, East Lansing, Michigan 48824, USA*

⁴*CEA, Centre de Saclay, IRFU/Service de Physique Nucléaire, F-91191 Gif-sur-Yvette, France*

⁵*Department of Physics, Ohio State University, Columbus, Ohio 43210, USA*

(Received 21 September 2010; published 11 November 2010)

In a recent series of articles, Gebremariam, Bogner, and Duguet derived a microscopically based nuclear energy density functional by applying the density matrix expansion (DME) to the Hartree-Fock energy obtained from chiral effective field theory two- and three-nucleon interactions. Owing to the structure of the chiral interactions, each coupling in the DME functional is given as the sum of a coupling constant arising from zero-range contact interactions and a coupling function of the density arising from the finite-range pion exchanges. Because the contact contributions have essentially the same structure as those entering empirical Skyrme functionals, a microscopically guided Skyrme phenomenology has been suggested in which the contact terms in the DME functional are released for optimization to finite-density observables to capture short-range correlation energy contributions from beyond Hartree-Fock. The present article is the first attempt to assess the ability of the newly suggested DME functional, which has a much richer set of density dependencies than traditional Skyrme functionals, to generate sensible and stable results for nuclear applications. The results of the first proof-of-principle calculations are given, and numerous practical issues related to the implementation of the new functional in existing Skyrme codes are discussed. Using a restricted singular value decomposition optimization procedure, it is found that the new DME functional gives numerically stable results and exhibits a small but systematic reduction of our test χ^2 function compared to standard Skyrme functionals, thus justifying its suitability for future global optimizations and large-scale calculations.

DOI: [10.1103/PhysRevC.82.054307](https://doi.org/10.1103/PhysRevC.82.054307)

PACS number(s): 21.10.-k, 21.30.-x, 21.60.Jz

I. INTRODUCTION

One of the fundamental challenges of nuclear theory is to predict properties of nuclei starting from the underlying vacuum two- and three-nucleon interactions. While impressive progress has been made in extending the limits of *ab initio* methods beyond the lightest nuclei [1–3], the nuclear energy density functional (EDF) approach is the only computationally feasible many-body method capable of describing nuclei across the mass table [4]. Driven by interest in the coming generation of radioactive isotope beam facilities, along with studies of astrophysical systems such as neutron stars and supernovae that require controlled extrapolations of nuclear properties in isospin, density, and temperature, there is a large effort currently under way to develop nuclear energy functionals with substantially reduced global errors and improved predictive power away from stability. The Universal Nuclear Energy Density Functional (UNEDF) SciDAC-2 collaboration

is one such effort that aims to develop a comprehensive theory of nuclear structure and reactions utilizing the most advanced computational resources and algorithms available, including high-performance computing techniques to scale to petaflop platforms and beyond [5].

Well-known empirical Skyrme and Gogny EDFs are typically characterized by 10–15 coupling constants adjusted to selected experimental data. Despite their simplicity, such functionals provide a remarkably good description of a broad range of bulk properties such as ground-state masses, separation energies, etc., and to a lesser extent of certain spectroscopic features of known nuclei. They are also widely employed, with some success, in studies of complex nuclear phenomena such as large-amplitude collective motion. However, their phenomenological nature often leads to parametrization-dependent predictions and does not offer a clear path toward systematic improvements.

One possible strategy is to provide microscopic constraints on the analytical form of the functional and the values of its couplings from many-body perturbation theory (MBPT) starting from the underlying two- (NN) and three-nucleon (NNN) interactions [6–12]. Recent progress in evolving chiral effective field theory (EFT) interactions to lower momentum using renormalization-group (RG) methods [13–17] (see also Refs. [18,19]) is expected to play a significant role in this effort, as the Hartree-Fock approximation becomes a reasonable

*stoitsovmv@ornl.gov

†kortelaine@ornl.gov

‡bogner@nscl.msu.edu

§thomas.duguet@cea.fr

||furnstahl.1@osu.edu

¶gebremar@nscl.msu.edu

**schuncknf@ornl.gov

(if not quantitative) starting point. This suggests that the theoretical developments and phenomenological successes of EDF methods for Coulomb systems may be applicable to the nuclear case for low-momentum interactions.

However, even with these simplifications, the MBPT energy expressions are written in terms of density matrices and propagators folded with finite-range interaction vertices and are therefore nonlocal in both space and time. To make such functionals numerically tractable in heavy open-shell nuclei, it is necessary to develop simplified approximations, for example, based on the use of local densities and currents. At lowest order in MBPT (i.e., Hartree-Fock), the density matrix expansion (DME) of Negele and Vautherin [20] provides a convenient framework for approximating the spatially nonlocal Fock energy as a local Skyrme-like functional with density-dependent couplings. This novel density dependence of the couplings is a consequence of the finite range of the vacuum interactions, and is controlled by the longest-ranged components. Consequently, the DME can be used to map physics associated with long-range one- and two-pion exchange interactions into a local EDF form that can be implemented at minimal cost in existing Skyrme codes. The rich spin and isospin structure of such interactions should improve the quantitative predictive power of EDFs while at the same time retaining the connection of these functionals with the underlying microscopic theory of nuclear forces.

We do not expect dramatic changes for bulk nuclear properties owing to the tendency of pions to average out in spin and isospin sums, but we do expect interesting consequences for single-particle properties (which phenomenology tells us are sensitive probes of the tensor force) and systematics along long isotopic chains (which should be sensitive to the isovector physics coming from pion-exchange interactions). Another potentially significant advantage of the DME functional is that two very different microscopic origins of spin-orbit properties (i.e., short-range NN and long-range NNN spin-orbit interactions) are treated on an equal footing. This is in contrast to empirical Skyrme and Gogny functionals, where the density-independent spin-orbit coupling is consistent with the short-range NN spin-orbit interaction but has no obvious connection with the subleading (but quantitatively significant) long-range NNN sources of spin-orbit physics. Although it is beyond the scope of the present article, let us mention that a clear priority of future studies will therefore be to examine if the DME-based functional is able to improve two major shortcomings of standard Skyrme phenomenology [21]: (i) the destructive interplay between tensor and spin-orbit terms that compromise spin-orbit splittings and the evolution of nuclear shell with isospin, and (ii) the too-high location of high- l centroids compared to low- l ones, which compromises the shell position even for nuclei near the stability valley. Any positive change regarding these two points would significantly impact the performance and predictive power of EDF calculations dedicated to spectroscopy.

Recently, Gebremariam *et al.* have used an improved formulation of the DME [22] to construct a nonempirical Hartree-Fock energy functional from unevolved chiral EFT two- and three-nucleon interactions through next-to-next-to-leading-order (N^2LO) [23,24]. The structure of the EFT

interactions implies that each coupling in the DME Hartree-Fock (HF) functional can be written as the sum of a density-independent (Skyrme-like) coupling constant arising from the zero-range contact interactions and a density-dependent coupling function arising from the long-range pion-exchange interactions. As discussed in Sec. II, in the present approach the separation of long- and short-distance physics at the HF level is used to motivate a semiphenomenological functional. In particular, the DME coupling functions arising from finite-range pion-exchanges are not modified, while the density-independent couplings associated with the contact interactions are released for optimization to infinite nuclear matter and finite nuclei properties to mimic higher-order short-range correlation energy contributions.

It is expected that the semiphenomenological DME-based functional should perform *at least* as well as empirical Skyrme functionals because one still fits the same Skyrme coupling constants to data, the only difference being that the new EDF contains additional parameter-free coupling functions derived from the finite-range NN and NNN interactions. However, owing to the highly nontrivial density dependence carried by the DME couplings, there is no *a priori* guarantee that the implementation will not be plagued with numerical instabilities or other technical difficulties that invalidate the approach. Consequently, the main goal of the present article is to perform “proof-of-principle” calculations in which we (i) give the practitioner’s view of how the DME functional can be implemented in existing Skyrme codes and (ii) perform a restricted singular value decomposition (SVD) optimization (“pre-optimization”) of the density-independent couplings to verify that the new microscopically guided phenomenology does no worse than standard Skyrme functionals, thus justifying its suitability for future global optimizations and large-scale EDF calculations.

In our initial investigation, we constrain zero-range volume parameters of the DME functional to reasonable values for equilibrium characteristics of infinite nuclear matter (INM), while zero-range surface parameters are obtained from a restricted optimization procedure using SVD techniques based on 72 even-even nuclei binding energies and 8 odd-even mass (OEM) differences (4 neutron and 4 proton). Our analysis shows that while the DME-based functional is indeed more susceptible to instabilities, it can still be made sufficiently stable to carry out an optimization procedure for nuclei throughout the nuclear mass chart. It should be stressed that a detailed comparison of the quality of the DME functional against standard Skyrme predictions and *a fortiori* experimental data is premature before applying a more rigorous global optimization.

The rest of the article is organized as follows. In Sec. II, we review how the DME can be used to map *ab initio* MBPT energy expressions into the form of a local EDF and motivate the semiphenomenological approach used in the present work. The explicit form of the functional is given in Sec. III, and the free parameters entering the volume part of the functional are expressed in terms of INM equilibrium characteristics in Sec. IV. The optimization procedure used to fix free surface parameters in the functional is described in Sec. V, and a comparison of selected nuclear properties calculated with both

the DME functional and the standard Skyrme functional is made in Sec. VI. Conclusions are given in Sec. VII, while various formulas and technical details are collected in the Appendixes.

II. MICROSCOPICALLY MOTIVATED FUNCTIONAL

A. DME exchange energy functional

At lowest order, the Fock energy computed from unevolved chiral interactions exhibits spatial nonlocalities owing to the convolution of finite-range form factors with nonlocal density matrices. The central idea of the DME is to factorize the nonlocality of the one-body density matrix (OBDM) by expanding it into a finite sum of terms that are separable in relative $\mathbf{r} \equiv \mathbf{r}_1 - \mathbf{r}_2$ and center of mass $\mathbf{R} \equiv (\mathbf{r}_1 + \mathbf{r}_2)/2$ coordinates. Adopting notations similar to those introduced in Refs. [22,23], one expands the spin-scalar and spin-vector parts (in both isospin channels) of the density matrix as

$$\rho_t(\mathbf{r}_1, \mathbf{r}_2) \approx \sum_{n=0}^{n_{\max}} \Pi_n(kr) \mathcal{P}_n(\mathbf{R}), \quad (1)$$

$$\mathbf{s}_t(\mathbf{r}_1, \mathbf{r}_2) \approx \sum_{m=0}^{m_{\max}} \Pi_m(kr) \mathcal{Q}_m(\mathbf{R}), \quad (2)$$

where k is an arbitrary momentum that sets the scale for the decay in the off-diagonal direction, whereas $\Pi_n(kr)$ denotes the so-called Π functions that depend on the particular formulation of the DME (see Refs. [22,23]). In the present work, k is chosen to be the local Fermi momentum related to the isoscalar density through

$$k \equiv k_F(\mathbf{R}) = \left(\frac{3\pi^2}{2} \rho_0(\mathbf{R}) \right)^{1/3}, \quad (3)$$

although other choices are possible that include additional τ and $\Delta\rho$ dependencies [25]. The functions $\{\mathcal{P}_n(\mathbf{R}), \mathcal{Q}_m(\mathbf{R})\}$ denote various local densities and their gradients $\{\rho_t(\mathbf{R}), \tau_t(\mathbf{R}), \mathbf{J}_t(\mathbf{R}), \nabla\rho_t(\mathbf{R}), \Delta\rho_t(\mathbf{R})\}$, which for time-reversal invariant systems are defined by

$$\rho_t(\mathbf{R}) \equiv \rho_t(\mathbf{r}_1, \mathbf{r}_2)|_{r_1=r_2=R}, \quad (4)$$

$$\tau_t(\mathbf{R}) \equiv \nabla_1 \cdot \nabla_2 \rho_t(\mathbf{r}_1, \mathbf{r}_2)|_{r_1=r_2=R}, \quad (5)$$

$$\mathbf{J}_t(\mathbf{R}) \equiv -\frac{i}{2} (\nabla_1 - \nabla_2) \times \mathbf{S}_t(\mathbf{r}_1, \mathbf{r}_2)|_{r_1=r_2=R}, \quad (6)$$

where the isospin index $t = \{0, 1\}$ labels isoscalar and isovector densities, respectively. For example, the isoscalar local density is the sum $\rho_0 = \rho_n + \rho_p$ of neutron ρ_n and proton ρ_p densities, while the isovector local density is the difference $\rho_1 = \rho_n - \rho_p$. Analogous expressions hold for τ_t, \mathbf{J}_t , and all other quantities labeled by the index $t = \{0, 1\}$.

Applying the expansion in Eqs. (1) and (2) to the nonlocal exchange (Fock) energy gives a spatial integral over a sum of bilinear and trilinear products of local densities. For time-reversal invariant systems (truncating the expansion to second-order in gradients), the NN exchange energy

becomes

$$E_x^{NN}[\rho] \approx \sum_{t=0,1} \int d\mathbf{R} \{ g_t^{\rho\rho} \rho_t^2 + g_t^{\rho\tau} \rho_t \tau_t + g_t^{\rho\Delta\rho} \rho_t \Delta\rho_t + g_t^{J\nabla\rho} \mathbf{J}_t \cdot \nabla\rho_t + g_t^{JJ} \mathbf{J}_t^2 \}, \quad (7)$$

while the NNN contribution yields

$$E_x^{3N}[\rho] \approx \int d\mathbf{R} \{ g^{\rho_0^3} \rho_0^3 + g^{\rho_0\rho_1^2} \rho_0 \rho_1^2 + g^{\rho_0^2\tau_0} \rho_0^2 \tau_0 + g^{\rho_1^2\tau_0} \rho_1^2 \tau_0 + g^{\rho_0\rho_1\tau_1} \rho_0 \rho_1 \tau_1 + g^{\rho_0^2\Delta\rho_0} \rho_0^2 \Delta\rho_0 + g^{\rho_1^2\Delta\rho_0} \rho_1^2 \Delta\rho_0 + g^{\rho_0\rho_1\Delta\rho_1} \rho_0 \rho_1 \Delta\rho_1 + g^{\rho_0 J_0^2} \rho_0 \mathbf{J}_0^2 + g^{\rho_0 J_1^2} \rho_0 \mathbf{J}_1^2 + g^{\rho_1 J_0 J_1} \rho_1 \mathbf{J}_0 \cdot \mathbf{J}_1 + g^{\rho_0 \nabla\rho_0 J_0} \rho_0 \nabla\rho_0 \cdot \mathbf{J}_0 + g^{\rho_0 \nabla\rho_1 J_1} \rho_0 \nabla\rho_1 \cdot \mathbf{J}_1 + g^{\rho_1 \nabla\rho_0 J_1} \rho_1 \nabla\rho_0 \cdot \mathbf{J}_1 + g^{\rho_1 \nabla\rho_1 J_0} \rho_1 \nabla\rho_1 \cdot \mathbf{J}_0 + g^{\rho_0^2 \nabla J_0} \rho_0^2 \nabla \cdot \mathbf{J}_0 + g^{\rho_1^2 \nabla J_0} \rho_1^2 \nabla \cdot \mathbf{J}_0 + g^{\rho_0\rho_1 \nabla J_1} \rho_0 \rho_1 \nabla \cdot \mathbf{J}_1 \}, \quad (8)$$

where, for simplicity, the \mathbf{R} dependence of the local densities and DME couplings has been omitted. The \mathbf{R} dependence [or equivalently, isoscalar density-dependence via Eq. (3)] of the couplings arises from the integral of the finite-range NN and NNN interactions over various products of the Π functions, for example,

$$g_t^{\rho\tau}(\mathbf{R}) \sim \int drr^2 \Pi_0^\rho(k_F r) \Pi_2^\tau(k_F r) \Gamma_c^{xt}(r), \quad (9)$$

where in this example $\Gamma_c^{xt}(r)$ is the central component of the exchange force $V(r)P_\sigma P_\tau$.

If the objective is to derive a fully microscopic and quantitative EDF free from any fitting to data, then the purely nonempirical HF functional of Ref. [23] is inadequate because unevolved chiral interactions generate too-strong coupling between low and high momenta for HF to be a reasonable zeroth-order approximation. Moreover, it is known that even if the interactions are softened by evolving to low momentum, it is still necessary to go to at least second-order MBPT to obtain a reasonable description of bulk properties of infinite matter as well as binding energies and charge radii of closed-shell nuclei.

Unfortunately, a consistent extension of the DME procedure beyond the HF level of MBPT has not yet been formulated. At this point in time, any attempt to microscopically construct a *quantitative* Skyrme-like EDF must therefore inevitably resort to either some *ad hoc* approximations (e.g., neglecting state-dependent energy denominators) when applying the DME to iterated contributions beyond the HF level and/or to the re-introduction of some phenomenological parameters to be adjusted to data [11,20,26–28]. An example of the latter approach has been recently proposed in Refs. [22,23].

B. Semiphenomenological DME functional

Schematically, the EFT NN and NNN potentials have the following structure:

$$V_{\text{EFT}} = V_\pi + V_{\text{ct}}, \quad (10)$$

where V_π denotes finite-range pion-exchange interactions and V_{ct} denotes scale-dependent zero-range contact terms

encoding the effects of integrated-out degrees of freedom (e.g., heavier meson exchanges, high-momentum two-nucleon states, etc.) on low-energy physics. Consequently, each DME coupling in Eqs. (7) and (8) decomposes into a density-independent coupling constant arising from the zero-range contact interactions and a density-dependent coupling function arising from long-range pion exchanges, for example,

$$g_i^{\rho\tau} \equiv g_i^{\rho\tau}(\mathbf{R}; V_\pi) + C_i^{\rho\tau}(V_{\text{ct}}), \quad (11)$$

and so on. Note that the zero-range V_{ct} generates HF contributions that are identical in form to the standard Skyrme functional, which is hardly surprising because such functionals were originally derived as the HF energy density resulting from a zero-range Skyrme “force” or pseudopotential.

Based on the clean separation between long- and short-distance physics at the HF level, a semiphenomenological approach where the long-distance couplings [$g_i^m(\mathbf{R}; V_\pi)$] are kept as is, and the zero-range C_i^m are optimized to finite nuclei and INM properties was suggested in Refs. [22,23]. While this is an admittedly empirical procedure, it is motivated by the observation that the dominant bulk correlations in nuclei and nuclear matter are primarily short-ranged in nature, as evidenced by Brueckner-Hartree-Fock (BHF) calculations where the Brueckner G matrix “heals” to the free-space interaction at sufficiently large distances.

Therefore, while a HF calculation using unevolved chiral NN and NNN interactions would provide a very poor description of nuclei, the application of the DME to such contributions nevertheless captures at least some of the nontrivial density dependencies that would arise from the finite-range tail of an in-medium vertex (e.g., a G matrix or a perturbative approximation thereof) that sums ladder diagrams in a more sophisticated many-body treatment. In this sense, one can loosely interpret the refit of the Skyrme constants to data as approximating the short-distance part of the G matrix with a zero-range expansion through second-order in gradients. In the following section, we describe how free parameters entering the volume part of the proposed functional can be fixed to equilibrium properties of infinite matter, while the remaining free surface parameters can be fixed to properties of nuclei using a restricted SVD optimization procedure.

III. IMPLEMENTATION OF THE DME FUNCTIONAL

A. Notations

We write the proposed semiphenomenological DME functional,

$$E[\rho] = \int \mathcal{H}(\mathbf{r}) d\mathbf{r}, \quad (12)$$

in the following form:

$$\mathcal{H}(\mathbf{r}) = \frac{\hbar^2}{2m} \tau_0 + \sum_{it'} \mathcal{H}_{it'}(\mathbf{r}), \quad (13)$$

$$\begin{aligned} \mathcal{H}_{it'}(\mathbf{r}) = & U_{it'}^{\rho^2} \rho_t \rho_{t'} + U_{it'}^{\rho\tau} \rho_t \tau_{t'} + U_{it'}^{J^2} \mathbf{J}_t \cdot \mathbf{J}_{t'} \\ & + U_{it'}^{\rho\Delta\rho} \rho_t \Delta\rho_{t'} + U_{it'}^{\rho\nabla J} \rho_t \nabla \cdot \mathbf{J}_{t'}, \end{aligned} \quad (14)$$

where the notation reflects that our attention is restricted to the ground states of even-even nuclei in the present article. Consequently, only terms built out of time-even densities are shown explicitly. The density dependence of the couplings has been omitted for brevity. Note that the strange “off-diagonal” isospin structure in Eq. (14) is a consequence of absorbing an extra factor of ρ_0 or ρ_1 into the definition of the $U_{it'}$ couplings, which allows the trilinear $3N$ contributions in Eq. (8) to be written in terms of the more familiar bilinear products of local densities, for example,

$$g^{\rho_1^2\tau_0} \rho_1^2 \tau_0 = \{g^{\rho_1^2\tau_0} \rho_1\} \rho_1 \tau_0 \equiv U_{10}^{\rho\tau} \rho_1 \tau_0, \quad (15)$$

and so on.

The $U_{it'}^m$ couplings (where m runs over the bilinears $\{\rho_t \rho_{t'}, \rho_t \tau_{t'}, \mathbf{J}_t \cdot \mathbf{J}_{t'}, \rho_t \Delta\rho_{t'}, \rho_t \nabla \cdot \mathbf{J}_{t'}\}$) have the following general structure:

$$U_{it'}^m = [C_t^m + g_t^m(u) + \rho_0 h_t^m(u)] \delta_{t,t'} + \rho_1 h_{it'}^m(u) (1 - \delta_{t,t'}), \quad (16)$$

where $u \equiv k_F(\mathbf{R})/m_\pi$. The functions $g_t^m(u)$ are obtained by applying the DME to the Fock-energy contributions from the finite-range pion-exchange parts of the chiral EFT NN interaction through N²LO. The functions $h_{it'}^m(u)$ and $h_t^m(u)$ originate from the finite-range part of the leading chiral NNN interaction (which appears at N²LO) and are related to the couplings in Eq. (8) by

$$h_t^m = \rho_0 g^{\rho_0 m}, \quad m \in \{\rho_t^2, \rho_t \tau_t, \rho_t \Delta\rho_t, \dots\}, \quad (17)$$

$$h_{it'}^m = \rho_1 g^{\rho_1 m}, \quad m \in \{\rho_t \rho_{t'}, \rho_t \tau_{t'}, \rho_t \Delta\rho_{t'}, \dots\}. \quad (18)$$

The C_t^m parameters correspond to the zero-range V_{ct} contributions, which, as discussed in the previous section, will be released for optimization. In this way, the proposed DME functional splits into two terms,

$$E[\rho] = E_{\text{ct}}[\rho] + E_\pi[\rho], \quad (19)$$

where the first term $E_{\text{ct}}[\rho] = E[\rho]_{g=h=0}$ collects all contributions from the contact part of the interaction plus higher-order short-range contributions encoded through the optimization to nuclei and nuclear matter, while the second term $E_\pi[\rho] = E[\rho]_{C_{it'}^n=0}$ collects the long-range NN and NNN pion exchange contributions at the HF level.

This leads to the following explicit form of the DME-based energy density

$$\mathcal{H}(\mathbf{r}) = \frac{\hbar^2}{2m} \tau_0 + \mathcal{H}_0(\mathbf{r}) + \mathcal{H}_1(\mathbf{r}) + \mathcal{H}_2(\mathbf{r}), \quad (20)$$

where, for $t = \{0, 1\}$,

$$\begin{aligned} \mathcal{H}_t(\mathbf{r}) = & [C_{t0}^{\rho^2} + C_{tD}^{\rho^2} \rho_0^\gamma + g_t^{\rho^2}(u) + \rho_0 h_t^{\rho^2}(u)] \rho_t^2 \\ & + [C_t^{\rho\tau} + g_t^{\rho\tau}(u) + \rho_0 h_t^{\rho\tau}(u)] \rho_t \tau_t \\ & + [C_t^{\rho\Delta\rho} + g_t^{\rho\Delta\rho}(u) + \rho_0 h_t^{\rho\Delta\rho}(u)] \rho_t \Delta\rho_t \\ & + [C_t^{\rho\nabla J} + g_t^{\rho\nabla J}(u) + \rho_0 h_t^{\rho\nabla J}(u)] \rho_t \nabla J_t \\ & + [C_t^{J^2} + g_t^{J^2}(u) + \rho_0 h_t^{J^2}(u)] J_t^2 \end{aligned} \quad (21)$$

and

$$\mathcal{H}_2(\mathbf{r}) = \rho_1 h_{10}^{\rho\tau}(u) \rho_1 \tau_0 + \rho_1 h_{10}^{\rho\Delta\rho}(u) \rho_1 \Delta\rho_0 + \rho_1 h_{10}^{J^2}(u) J_1 J_0 + \rho_1 h_{10}^{\rho\nabla J}(u) \rho_1 \nabla J_0. \quad (22)$$

The explicit forms of the functions $g_t^m(u)$ and $h_{tt'}^m(u)$ have been given in Ref. [23] and the companion MATHEMATICA notebooks. To gain a feeling about the new density dependencies entering through such couplings, we provide stripped-down “skeleton expressions” along with several explicit examples in Appendix A.

To facilitate the use of the DME functional in nuclear EDF calculations, we have also developed a general module written in FORTRAN 90 [29], which can easily be ported to any existing EDF solver. It contains all of the lengthy expressions for the DME couplings $U_{tt'}^m$ [Eq. (16)], their functional derivatives with respect to the density matrix, and numerically stable approximate expressions at small u . The module also has the capability to calculate related INM properties.

B. Contact part

The contact part $E_{\text{ct}}[\rho]$ has the form of the standard Skyrme functional

$$\mathcal{H}_{\text{ct}}(\mathbf{r}) = \frac{\hbar^2}{2m} \tau_0 + \mathcal{H}_0^{\text{ct}}(\mathbf{r}) + \mathcal{H}_1^{\text{ct}}(\mathbf{r}), \quad (23)$$

where

$$\mathcal{H}_t^{\text{ct}}(\mathbf{r}) = (C_{t0}^{\rho^2} + C_{tD}^{\rho^2} \rho_0^\gamma) \rho_t^2 + C_t^{\rho\tau} \rho_t \tau_t + C_t^{\rho\Delta\rho} \rho_t \Delta\rho_t + C_t^{\rho\nabla J} \rho_t \nabla J_t + C_t^{J^2} J_t^2. \quad (24)$$

This is illustrated in Appendix B, where the link between the coupling constants and the historical (t_n, x_n) parameterization of Skyrme “forces” is explicitly given.

As for the standard Skyrme functional, Eq. (23) contains 13 parameters,

$$\{C_{t0}^{\rho^2}, C_{tD}^{\rho^2}, C_t^{\rho\Delta\rho}, C_t^{\rho\tau}, C_t^{J^2}, C_t^{\rho\nabla J}, \gamma\}, \quad (25)$$

which are to be released for optimization to infinite matter and finite nuclei properties. While these parameters have exactly the same form as in the standard Skyrme functional, the existence of the long-range part in the functional will obviously modify their optimized values.

C. The parameter γ

Early versions of the Skyrme functional motivated the ρ^γ term appearing in Eq. (24) as arising from a zero-range NNN force, in which case $\gamma \equiv 1$. However, this interpretation was soon found to be problematic, as $\gamma = 1$ yields too large an incompressibility [4]. Subsequent Skyrme parametrizations largely cured this difficulty by letting γ float, with values typically between 1/6 and 1/3.

In EFT studies of dilute Fermi systems interacting with zero-range interactions, one finds similar noninteger powers of ρ appearing in the energy density, which can be traced to correlation (i.e., beyond HF) effects [30]. Even in this much simpler model system, where a controlled and well-defined EFT expansion is possible, it is interesting to note that one finds *multiple* noninteger powers of ρ occurring at low orders in the

expansion. Given that the nuclear many-body problem is much more complicated, with many additional possible sources of nonanalytic behavior owing to the interplay of finite-range NN and NNN interactions and short-range correlation effects analogous to those found in the dilute fermion system, the single noninteger ρ^γ term in Eq. (23) is probably not justified on microscopic grounds.

Nevertheless, in the short term we follow standard practice with a single ρ^γ term in the functional, which in our case can be loosely viewed as parameterizing the HF contribution of the NNN contact term, plus higher-order correlation effects that are implicitly included in the refit to data. However, ultimately one would like to revisit this issue to see if MBPT can be used to provide insight regarding the form of such nonanalytic terms.

D. Finite-range part

The finite-range part $E^\pi[\rho]$ follows from

$$\mathcal{H}_\pi(\mathbf{r}) = \mathcal{H}_0^\pi(\mathbf{r}) + \mathcal{H}_1^\pi(\mathbf{r}) + \mathcal{H}_2^\pi(\mathbf{r}), \quad (26)$$

where, for $t = \{0, 1\}$,

$$\begin{aligned} \mathcal{H}_t^\pi(\mathbf{r}) = & [g_t^{\rho^2}(u) + \rho_0 h_t^{\rho^2}(u)] \rho_t^2 + [g_t^{\rho\tau}(u) + \rho_0 h_t^{\rho\tau}(u)] \rho_t \tau_t \\ & + [g_t^{\rho\Delta\rho}(u) + \rho_0 h_t^{\rho\Delta\rho}(u)] \rho_t \Delta\rho_t \\ & + [g_t^{J^2}(u) + \rho_0 h_t^{J^2}(u)] J_t^2 \\ & + [g_t^{\rho\nabla J}(u) + \rho_0 h_t^{\rho\nabla J}(u)] \rho_t \nabla J_t, \end{aligned} \quad (27)$$

and

$$\mathcal{H}_2^\pi(\mathbf{r}) = \rho_1 h_{10}^{\rho\tau}(u) \rho_1 \tau_0 + \rho_1 h_{10}^{\rho\Delta\rho}(u) \rho_1 \Delta\rho_0 + \rho_1 h_{10}^{J^2}(u) J_1 J_0 + \rho_1 h_{10}^{\rho\nabla J}(u) \rho_1 \nabla J_0. \quad (28)$$

Couplings entering $E^\pi[\rho]$ are entirely determined in terms of the finite-range NN and NNN interaction parameters and are therefore frozen during the optimization procedure. In the present work, the values for the couplings that enter the finite-range chiral EFT interactions are taken from Ref. [31].

E. Hartree NN contributions

In general, it is possible to apply the DME to both Hartree and Fock energies so that the complete HF energy is mapped into a local functional. It is known since the original work of Negele and Vautherin, however, that treating the Hartree contributions exactly provides a better reproduction of the density fluctuations and the energy produced from an exact HF calculation [26,32]. Restricting the DME to the exchange contribution significantly reduces the self-consistent propagation of errors [26]. Moreover, treating the Hartree contribution exactly generates no additional complexity in the numerical solutions of the resulting self-consistent equations compared to applying the DME to both Hartree and Fock terms. Lending further support to Negele and Vautherin’s conclusions, we find that the present DME-based functional becomes extremely susceptible to numerical instabilities when the DME approximation is used for the Hartree terms, which immediately disappear when the Hartree terms are treated exactly.

In the present work, a simplification is used such that finite-range NN Hartree contributions are treated in the local density approximation (LDA). An exact treatment of these contributions and their influence on the results will be examined in a future investigation of the DME-based functional.

IV. CONSTRAINING THE VOLUME-TERM PARAMETERS

A. INM with the DME-based functional

We turn now to a discussion of how equilibrium properties of INM can be used to fix the seven free volume parameters $\{C_t^{\rho^2}, C_{tD}^{\rho^2}, C_t^{\rho\tau}, \gamma\}$ in the functional. In INM, the total energy per particle defines the saturation curve $W(\rho_n, \rho_p)$. Its derivation discards the Coulomb energy and all gradient terms that are zero for a homogeneous system and substitutes the kinetic energy density with its Thomas-Fermi expression, which is exact in this case. Assuming spin saturation, one also disregards the terms involving the spin-orbit current density, \mathbf{J}_t .

The expansion of $W(\rho_n, \rho_p)$ around the equilibrium density ρ_c in a Taylor series in $\rho = \rho_n + \rho_p$ and $I \equiv (\rho_n - \rho_p)/\rho$ yields

$$W(\rho, I) = W(\rho) + S_2(\rho)I^2 + S_4(\rho)I^4, \quad (29)$$

$$W(\rho) = \frac{E^{\text{NM}}}{A} + \frac{P^{\text{NM}}}{\rho_c^2}\delta\rho + \frac{K^{\text{NM}}}{18\rho_c^2}(\delta\rho)^2, \quad (30)$$

$$S_2(\rho) = a_{\text{sym}}^{\text{NM}} + \frac{L^{\text{NM}}}{3\rho_c}\delta\rho + \frac{\Delta K^{\text{NM}}}{18\rho_c^2}(\delta\rho)^2, \quad (31)$$

where $\delta\rho = (\rho - \rho_c)$, while E^{NM}/A , P^{NM} , K^{NM} , $a_{\text{sym}}^{\text{NM}}$, L^{NM} , and ΔK^{NM} denote the total energy per nucleon at equilibrium, the pressure, the nuclear matter incompressibility, the symmetry energy coefficient, the density derivative of $a_{\text{sym}}^{\text{NM}}$, and the isovector correction to the incompressibility at saturation density ρ_c of nuclear matter, respectively. The quartic term in I can be safely neglected in Eq. (29) in practice.

The INM equation of state (EOS) following from the functional Eq. (14) takes the form

$$\begin{aligned} W(I, \rho) = & \frac{\hbar^2}{2m}\tau_0 + [C_{00}^{\rho^2} + C_{0D}^{\rho^2}\rho^\gamma + g_0^{\rho^2}(u) + \rho h_0^{\rho^2}(u)]\rho \\ & + [C_{10}^{\rho^2} + C_{1D}^{\rho^2}\rho^\gamma + g_1^{\rho^2}(u) + \rho h_1^{\rho^2}(u)]I^2\rho \\ & + [C_0^{\rho\tau} + g_0^{\rho\tau}(u) + \rho h_0^{\rho\tau}(u) + I^2\rho h_{10}^{\rho\tau}(u)]\tau_0 \\ & + [C_1^{\rho\tau} + g_1^{\rho\tau}(u) + \rho h_1^{\rho\tau}(u)]I\tau_1, \end{aligned} \quad (32)$$

where

$$u = \frac{k_F}{m_\pi} = \frac{1}{m_\pi} \left(\frac{3\pi^2}{2} \right)^{1/3} \rho^{1/3}, \quad (33)$$

$$\tau_0 = \frac{1}{2}C\rho^{2/3}[(1+I)^{5/3} + (1-I)^{5/3}], \quad (34)$$

$$\tau_1 = \frac{1}{2}C\rho^{2/3}[(1+I)^{5/3} - (1-I)^{5/3}], \quad (35)$$

$$C = \frac{3}{5} \left(\frac{3\pi^2}{2} \right)^{2/3}. \quad (36)$$

Our strategy is to express unknown volume parameters in terms of nuclear matter equilibrium quantities ρ_c , E^{NM}/A , K^{NM} , $a_{\text{sym}}^{\text{NM}}$, L^{NM} , m_s^* , and m_v^* , where m_s^* and m_v^* are the isoscalar and isovector effective masses, respectively. This strategy has been recently applied in the context of the optimization of pure Skyrme functionals [33].

B. Symmetric nuclear matter constraints

Symmetric nuclear matter (SNM) is characterized by equal neutron and proton densities $\rho_n = \rho_p = \rho/2$, where ρ is the isoscalar density. All isovector terms are thus zero. The isoscalar kinetic energy density per particle from Eq. (34) is

$$\tau = C\rho^{2/3}. \quad (37)$$

Parameters $C_{00}^{\rho^2}$, $C_{0D}^{\rho^2}$, and $C_0^{\rho\tau}$ are then expressed in terms of E^{NM}/A , ρ_c , and m_s^* through

$$\begin{aligned} C_{00}^{\rho^2} = & \frac{1}{3\gamma\rho_c} \left\{ 3(\gamma+1)\frac{E^{\text{NM}}}{A} - \frac{\hbar^2}{2m} \right. \\ & \left. \times [3 - (2 - 3\gamma)m_s^{*-1}] \tau_c + A_{00}(u_c) \right\}, \end{aligned} \quad (38)$$

$$C_{0D}^{\rho^2} = \frac{1}{3\gamma\rho_c^{\gamma+1}} \left[-3\frac{E^{\text{NM}}}{A} - \frac{\hbar^2}{2m}(2m_s^{*-1} - 3)\tau_c + A_{0D}(u_c) \right], \quad (39)$$

$$C_0^{\rho\tau} = \frac{\hbar^2}{2m}(m_s^{*-1} - 1)\frac{1}{\rho_c} - g_0^{\rho\tau}(u_c) - h_0^{\rho\tau}(u_c)\rho_c, \quad (40)$$

where τ_c and u_c are the kinetic energy density and the dimensionless Fermi momentum at the saturation density ρ_c , respectively. Explicit expressions for $A_{t0}(u)$ and $A_{tD}(u)$ are given in Appendix C.

As for the parameter γ , one can either leave it as a free parameter or eliminate it using the incompressibility K^{NM} . The resulting expression is

$$\gamma = \frac{-K^{\text{NM}} - 9E^{\text{NM}}/A + \frac{\hbar^2}{2m}(4m_s^{*-1} - 3)\tau_c + A_\gamma(u_c)}{9E^{\text{NM}}/A + 3\frac{\hbar^2}{2m}(2m_s^{*-1} - 3)\tau_c + B_\gamma(u_c)}, \quad (41)$$

where explicit expressions for $A_\gamma(u_c)$ and $B_\gamma(u_c)$ are given in Appendix C.

C. Asymmetric nuclear matter constraints

In the regime of isospin-asymmetric INM, neutron and proton densities are different ($\rho_0 = \rho$, $\rho_1 = I\rho$) and the isovector terms contribute. One can therefore express parameters $C_{10}^{\rho^2}$, $C_{1D}^{\rho^2}$, and $C_1^{\rho\tau}$ in terms of $a_{\text{sym}}^{\text{NM}}$, L^{NM} , and m_v^* through

$$\begin{aligned} C_{10}^{\rho^2} = & \frac{27(\gamma+1)a_{\text{sym}}^{\text{NM}} - 9L^{\text{NM}} + 20(2-3\gamma)C_0^{\rho\tau}\rho_c\tau_c}{27\gamma\rho_c} \\ & + \frac{\hbar^2}{2m} \left[(9\gamma - 6)m_v^{*-1} - 12\gamma + 5 \right] \tau_c + A_{10}(u), \end{aligned} \quad (42)$$

$$C_{1D}^{\rho^2} = \frac{-27a_{\text{sym}}^{\text{NM}} + 9L^{\text{NM}} - 40C_0^{\rho\tau} \rho_c \tau_c}{27\gamma\rho_c^{\gamma+1}} + \frac{\frac{\hbar^2}{2m}(30m_v^{*-1} - 25)\tau_c + A_{1D}(u)}{27\gamma\rho_c^{\gamma+1}}, \quad (43)$$

$$C_1^{\rho\tau} = \frac{\hbar^2}{2m}(m_s^{*-1} - m_v^{*-1}) \frac{1}{\rho_c} - g_1^{\rho\tau}(u) - h_1^{\rho\tau}(u)\rho_c, \quad (44)$$

where $C_0^{\rho\tau}$ has already been determined by Eq. (40).

D. Reference SLy4 properties

In this work, we often use as a benchmark the SLy4 parametrization of the Skyrme force [34]. The optimization protocol of this interaction included data obtained from *ab initio* calculations in nuclear matter of Ref. [35], and we see in Fig. 1 that the saturation curves obtained with SLy4 agree well with the *ab initio* results. We therefore take the INM equilibrium characteristics of the SLy4 parametrization as an

acceptable set of values to be used in Eqs. (38)–(44),

$$\begin{aligned} \frac{E^{\text{NM}}}{A} &= -15.97 \text{ MeV}, & \rho_c &= 0.1595 \text{ fm}^{-3}, \\ K^{\text{NM}} &= 229.9 \text{ MeV}, & m_{s/v}^{*-1} &= 1.44/1.25, \\ a_{\text{sym}}^{\text{NM}} &= 32.0 \text{ MeV}, & L^{\text{NM}} &= 45.96 \text{ MeV}. \end{aligned} \quad (45)$$

The resulting parameters $C_{t0}^{\rho^2}$, $C_{tD}^{\rho^2}$, $C_t^{\rho\tau}$, and γ are compared with the original SLy4 parameters in Table I, and the associated INM curves are shown in Fig. 1 for symmetric matter (top panel) and pure neutron matter (bottom panel).

As seen in Table I, the values of the refitted parameters differ substantially from the original SLy4 values. The original value of $\gamma = 1/6$, for example, increases to about $\gamma = 1/3$ when only NN contributions are taken into account, but becomes almost equal to one when both NN and NNN contributions are accounted for at the $N^2\text{LO}$ level. Nevertheless, the EOS for the DME-based functional are practically identical to the original SLy4 curves for symmetric (top panel of Fig. 1) and pure neutron matter (bottom panel of Fig. 1) for densities relevant to nuclei.

At higher densities ($\rho > 0.3 \text{ fm}^{-3}$) the symmetric matter EOS (Fig. 1, top) remains completely predetermined by the imposed equilibrium values [Eq. (45)] with a slight deviation toward the reference points when NNN contributions are taken into account ($N^2\text{LO}$). Deviations in this density range become more visible for the neutron matter EOS (Fig. 1, bottom), as isovector properties depend on the EFT order and/or whether the NNN force is taken into account ($N^2\text{LO}$) or not ($N^2\text{LO}^{NN}$).

If one does not impose the nuclear incompressibility value $K^{\text{NM}} = 229.9 \text{ MeV}$ but instead varies the value of γ , one can trace the influence of the DME contributions on the INM incompressibility K^{NM} . Such results are shown in Table II for two values of γ : $\gamma = 1/6$, corresponding to the SLy4 parametrization, and $\gamma = 1$, originally proposed for Skyrme functionals [36].

Contributions from the NN interaction generally reduce the value of K^{NM} by about 10–20 MeV. Conversely, NNN contributions give too-high values for K^{NM} unless $\gamma \sim 1$, which brings the $N^2\text{LO}$ K^{NM} value to the physically accepted range of 220–250 MeV. Interestingly, the fact that the preferred value of γ is rather close to 1 when finite-range NNN contributions are explicitly accounted for seems to contradict the naive argument recalled in Sec. III C that γ should encode both the HF contribution of the NNN contact term ($\gamma = 1$) but also higher-order correlation effects producing noninteger values for γ .

E. First test on surface parameters

The equilibrium INM properties allow us to constrain the zero-range volume parameters of the DME-based functional (Table I), but not the parameters $C_t^{\rho\Delta\rho}$ and $C_t^{\rho\nabla J}$ entering the surface part of the functional or the tensor parameters $C_t^{J^2}$ as their associated terms are zero in spin-symmetric nuclear matter. We note right away that all tensor terms from both pion exchanges and the Skyrme-like contact terms are omitted in

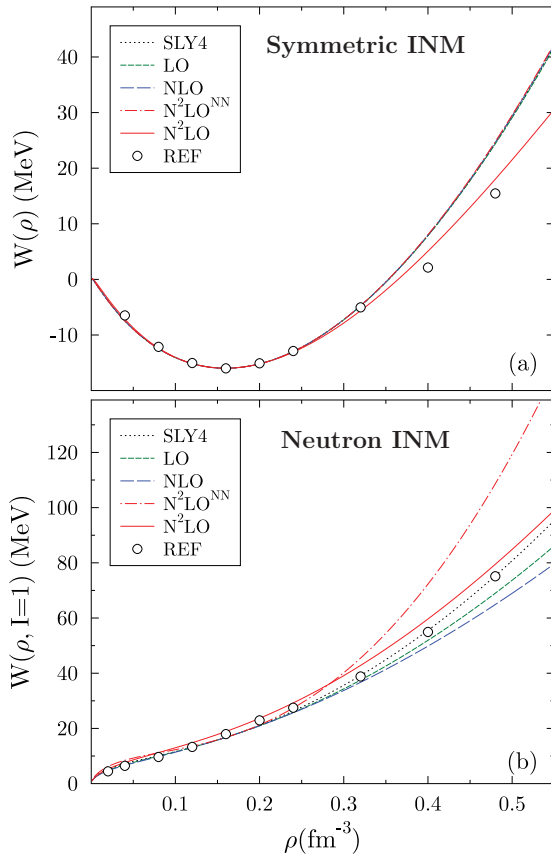


FIG. 1. (Color online) INM saturation curves for symmetric (a) and neutron (b) nuclear matter calculated with the standard SLy4 Skyrme functional (dotted lines), and the DME functional at LO (dashed lines), NLO (dot-dashed lines), $N^2\text{LO}$ without NNN contributions (short-dashed lines), and $N^2\text{LO}$ (solid lines). *Ab initio* results [35] are plotted as reference points. All functionals are constrained to reproduce the reference INM saturation values from Eq. (45).

TABLE I. Parameters entering the volume part of the standard Skyrme functional and the DME functional at LO, NLO, N²LO without NNN contributions (N²LO ^{NN}), and N²LO, all reproducing the same values Eq. (45) for INM saturation properties.

Parameters	SLy4	LO	NLO	N ² LO ^{NN}	N ² LO
$C_{00}^{\rho^2}$	-933.342	-727.093	-757.689	-777.805	-607.108
$C_{10}^{\rho^2}$	830.052	477.931	477.931	677.296	331.438
$C_{0D}^{\rho^2}$	861.062	612.114	628.504	641.017	-1082.85
$C_{1D}^{\rho^2}$	-1064.273	-705.739	-694.665	-952.381	-4383.27
$C_0^{\rho\tau}$	57.129	33.885	18.471	26.0411	322.4
$C_1^{\rho\tau}$	24.657	32.405	92.233	-51.8352	-156.90
γ	0.16 667	0.30 622	0.287 419	0.275 049	1.06 429

the present proof-of-principle investigation. The reasons for that are briefly discussed in Sec. V.

As for a first test on the surface parameters of the DME-based functional, we keep the volume ones at the values estimated from INM (Table I), and simply set $C_t^{\rho\Delta\rho}$ and $C_t^{\rho\nabla J}$ equal to zero. That is, we let the long-range DME part of the functional ($E_\pi[\rho]$) generate all of the surface contributions. Results of such calculations at LO for two benchmark nuclei ⁴⁰Ca and ²⁰⁸Pb are shown in the second column of Table III. The comparison with the results by SLy4 (the first column in Table III) shows unacceptable overbinding of about 140 and 320 MeV in ⁴⁰Ca and ²⁰⁸Pb, respectively.

As a second test case, we compute the LO DME results in which we have taken the SLy4 values for $C_t^{\rho\Delta\rho}$ and $C_t^{\rho\nabla J}$ (third column on Table III). In this case, the results are much closer but now an underbinding of about 10 and 30 MeV is seen in ⁴⁰Ca and ²⁰⁸Pb, respectively.

Table III suggests that it should be possible to optimize the surface parameters in the DME functional in a manner similar to the optimization done for standard Skyrme functionals. Broadly speaking, one could think of procedures based on semi-infinite NM properties, or on the leptodermous expansion of the functional. Both approaches would fix the parameters entering the surface part of the functional on a set of well-defined surface coefficients. Alternatively, one can probe and constrain the surface parameters using properties of finite nuclei. This is the path taken in the present work and described in Sec. V.

F. Stability of the DME-based functional

Our preliminary analysis of calculations using different sets of C_t^m parameters has shown that the DME functional is somewhat more sensitive to instabilities than standard Skyrme

TABLE II. Nuclear matter incompressibility K^{NM} (in MeV) calculated at two different values of γ .

	SLy4	LO	NLO	N ² LO ^{NN}	N ² LO
$\gamma = 1/6$	229.90	208.49	211.42	213.34	440.50
$\gamma = 1$	356.36	336.34	338.96	340.68	244.98

functionals, especially when the N²LO NNN contributions are taken into account. Nevertheless, we have been able to sidestep these issues thus far with minimal modifications.

The DME procedure, for example, contains a freedom in the choice of the coordinate system when expanding the OBDM with respect to the center-of-mass coordinate [37]. This freedom introduces a factor ($a^2 - a + 1/2$) in front of the surface terms proportional to $\rho\Delta\rho$, with a ranging between zero and one. In quantum chemistry studies of molecular exchange energies, taking $a = 0$, which corresponds to expanding $\rho(\mathbf{r}_1, \mathbf{r}_2)$ asymmetrically about \mathbf{r}_2 , was found to be the optimal choice by a large margin [37]. For nuclei, we find that the quantum chemistry choice leads to overly strong surface contributions, resulting in heavy underbinding, which can only be compensated by substantially reducing the associated surface constants $C_t^{\rho\Delta\rho}$. Such a reduction, however, leads to

TABLE III. Comparison of calculated SLy4 energies (in MeV) with the results from DME calculations at LO for nuclei ⁴⁰Ca and ²⁰⁸Pb, kinetic energy for neutrons T_n and protons T_p , volume energy E_V , surface energy E_S (see also Table IV), and total energy E_T . Volume DME parameters are taken from Table II. Surface DME parameters $C_t^{\rho\Delta\rho}$ and $C_t^{\rho\nabla J}$ are set equal to zero (third column) or to their SLy4 values (fourth column).

	SLy4	$C_t^{\rho\Delta\rho}$ and $C_t^{\rho\nabla J} = 0$ DME:LO	From SLy4 DME:LO
⁴⁰ Ca			
T_n	321.788	401.334	313.497
T_p	313.215	393.286	304.782
E_V	-1161.116	-1362.847	-1130.494
E_S	111.046	7.889	109.992
E_T	-344.227	-480.770	-332.150
²⁰⁸ Pb			
T_n	2527.799	2819.082	2490.574
T_p	1336.341	1481.145	1321.254
E_V	-6514.517	-7092.892	-6429.071
E_S	315.116	65.083	316.181
E_T	-1635.160	-1950.690	-1599.798

numerical instabilities of the HFB solution for practically all nuclei studied.

In our test calculations, we are able to avoid such difficulties by using the original Negele-Vautherin choice ($a = 1/2$), which corresponds to symmetrically expanding $\rho(\mathbf{r}_1, \mathbf{r}_2)$ about the center-of-mass coordinate $\mathbf{R} = (\mathbf{r}_1 + \mathbf{r}_2)/2$. This choice minimizes the long-range $\rho\Delta\rho$ contributions and leads to stable results for the nuclei studied in the present article.

Another source of instabilities has been found with respect to the isovector behavior of the DME-based functional. For example, increasing the value of the symmetry energy parameter $a_{\text{sym}}^{\text{NM}}$ generates a functional that has an instability that cannot be compensated by the contact part of the functional. As a matter of fact, the N^2LO functional displays systematic instabilities in finite nuclei calculations when it is defined with the values of Table II. However, by slightly modifying the values of INM characteristics to $a_{\text{sym}}^{\text{NM}} = 30$ MeV and $L^{\text{NM}} = 40$ MeV [compare with values in Eq. (45)], the N^2LO functional becomes stable enough to carry out the SVD optimization of the surface parameters as discussed in the next section. The resulting EOS in both symmetric and pure neutron matter are shown in Fig. 2, where one sees that the latter is much better behaved at high density as one increases the EFT order.

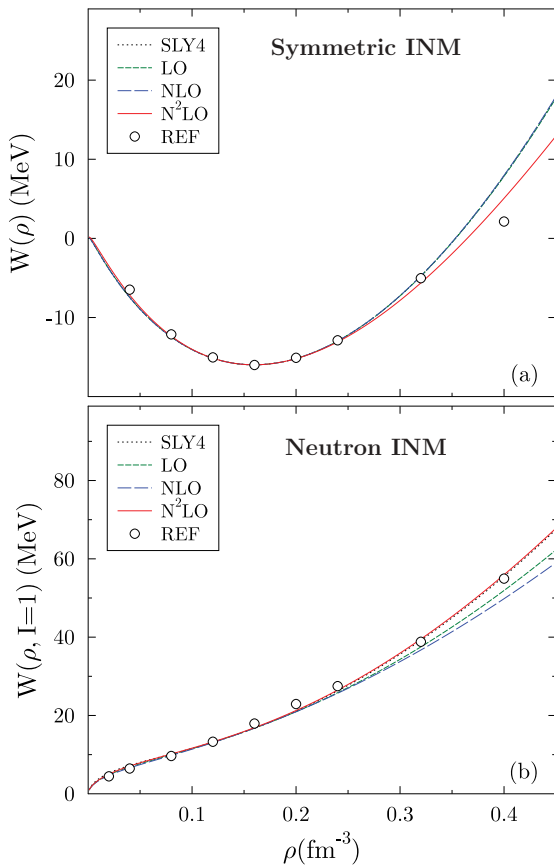


FIG. 2. (Color online) INM saturation curves for symmetric (a) and neutron (b) nuclear matter calculated with the modified SLy4' Skyrme functional (dotted lines) and the DME functional at LO (dashed lines), NLO (dot-dashed lines), and N^2LO (solid lines) using the parameters from Table IV.

In the calculations presented in what follows, we have managed thus far to avoid such instabilities in our zeroth-order optimization (“pre-optimization”) to fix the volume and surface parameters of the DME-based functional. However, a more sophisticated global optimization of the DME-based functional will ultimately require a more precise and detailed analysis of its stability properties to rule out the most common problems [38].

V. PRE-OPTIMIZATION

A global optimization of a given EDF parametrization becomes a very involved procedure as soon as one extends the data set to include observables beyond nuclear binding energies. Such optimization procedures are expensive, as they require a large number of functional evaluations. It is always useful for the global optimization to have preliminary estimates for the values of the functional parameters.

The SVD optimization method used in our work utilizes the explicit linear dependence of the functional on the parameters C_t^m . This procedure can be seen as a particular implementation of the optimization algorithm based on the regression analysis of Refs. [39,40].

In our optimization procedure we used the same χ^2 function as in Ref. [33], with one exception. Owing to the limitations of the employed SVD optimization method, we did not use proton radii. The pairing functional used in the present work was a mixed δ pairing [41], similar to the one in Ref. [33].

Besides the adjustment to binding energies and OEM differences, it is necessary to impose boundaries to the domain of variation of the free parameters owing to the approximate nature of the nuclear functional and the incomplete set of experimental observables used. For example, one cannot release for optimization parameters $C_t^{\rho\nabla J}$ controlling spin-orbit contributions simultaneously with parameters $C_t^{J^2}$ governing tensor contributions [21]. In the present proof-of-principle investigation, we drop all tensor contributions from pion exchanges entering the DME-based functional. That is, the amplitudes $U_{tt'}^{JJ}$ are set to zero so that we can avoid optimizing the corresponding contact terms. Eventually, such terms will be subject to detailed investigation for the reasons explained in the Introduction. Even then, all remaining parameters C_t^m cannot be fully released for a SVD optimization. Such attempts lead to a negative isovector effective mass (experimental data cannot constrain this quantity [33]) or to a too-small INM saturation density (charge radii are not included in the present optimization).

The SVD optimization procedure has been performed with respect to the six parameters $C_0^{\rho\Delta\rho}$, $C_1^{\rho\Delta\rho}$, $C_0^{\rho\nabla J}$, $C_1^{\rho\nabla J}$, V_n , and V_p using the binding energies of 30 spherical and 42 deformed nuclei, neutron pairing gaps of 4 nuclei, and proton pairing gaps of another 4 nuclei. Nuclear properties have been calculated as in Ref. [33] using the HFBTHO solver [42] in the Lipkin-Nogami regime of approximate particle number projection [43]. For comparison, the same SVD optimization procedure has also been performed for the standard Skyrme functional starting from the SLy4 parametrization. The results define a new parametrization referred to as SLy4'.

TABLE IV. Parameters entering the volume, surface, and pairing parts of the standard Skyrme functional and the DME-based functional at LO, NLO, and N²LO. The associated χ^2 values and RMSDs are also shown.

Parameter	SLy4	SLy4'	LO	NLO	N ² LO
Volume parameters					
$C_{00}^{\rho^2}$	-933.342		-727.093	-757.689	-607.108
$C_{10}^{\rho^2}$	830.052		474.871	477.931	316.939
$C_{0D}^{\rho^2}$	861.062		612.104	628.504	-1082.854
$C_{1D}^{\rho^2}$	-1064.273		-705.739	-694.665	-4369.425
$C_0^{\rho\tau}$	57.129		33.885	18.471	322.4
$C_1^{\rho\tau}$	24.657		32.405	92.233	-156.901
γ	0.16667		0.30622	0.287419	1.06429
Surface parameters					
$C_0^{\rho\Delta\rho}$	-76.287	-76.180	-67.437	-63.996	-197.132
$C_1^{\rho\Delta\rho}$	15.951	24.823	21.551	-9.276	-12.503
$C_0^{\rho\nabla J}$	-92.250	-92.959	-95.451	-95.463	-193.188
$C_1^{\rho\nabla J}$	-30.75	-82.356	-65.906	-60.800	37.790
Pairing parameters					
V_n	-258.992	-232.135	-241.203	-241.484	-272.164
V_p	-258.992	-244.050	-252.818	-252.222	-286.965
SVD optimization results					
χ^2	12.5002	2.1235	1.837	1.7662	1.7884
$(E)_{\text{RMSD}}$	7.008	2.6931	2.5539	2.5143	2.590
$(\Delta_n)_{\text{RMSD}}$	0.1297	0.0828	0.0587	0.0554	0.0476
$(\Delta_p)_{\text{RMSD}}$	0.094	0.0988	0.0902	0.0866	0.0706

The values of the parameters resulting from the SVD optimization, together with the χ^2 values and the resulting root-mean-square deviations (RMSDs), are shown in Table IV. The second column in Table IV shows the results for SLy4. Because our HFBTHO calculations are performed under the Lipkin-Nogami procedure, SLy4 leads to quite a high value of $\chi^2 \approx 12.5$. The third column in Table IV shows the results for SLy4'. The resulting χ^2 is about six times smaller, $\chi^2 \approx 2.12$.

The optimal DME-based functional further reduces the value of χ^2 , but by a much less significant amount. This is nevertheless a remarkable result, keeping in mind the extremely involved structure, that is, the rich density dependence of the coupling functions, of the DME contributions and the fact that they do not contain optimization parameters. Interestingly, the N²LO parametrization (last column of Table IV) performs as well as standard Skyrme functionals with a reasonable incompressibility $K^{\text{NM}} = 230$ MeV, even though its contact part is characterized by a density-dependent power $\gamma \sim 1$.

Because the DME-based functional is found to provide as good (or slightly better) a description of bulk properties of finite nuclei as standard Skyrme functionals, a refined (and much more costly) global optimization can be undertaken that will eventually lead to a systematic analysis of its ability to improve the known deficiencies of standard functionals. Such a task is left for a future work. With a much less ambitious objective in mind, the following section gives some insight into the novelties that could be expected from DME functionals in

typical nuclear structure applications by collecting a sample of results obtained with the parametrization of Table IV.

VI. SELECTED RESULTS IN FINITE NUCLEI

This section summarizes results for selected nuclei, comparing their properties calculated with the standard Skyrme functional (SLy4' set of parameters) and the DME-based functional with the parameters given in Table IV. Let us recall again that a detailed comparison of the DME functional to experimental data is premature until a more rigorous global optimization is performed.

As the first example, Fig. 3 compares experimental single-particle energies of [44] for the nucleus ²⁰⁸Pb with the canonical single-particle energies calculated with SLy4' and the LO, NLO, and N²LO DME functionals. In general, the comparison shows that the DME functional does not modify the Skyrme results significantly. The largest deviations are seen in the N²LO case mainly owing to the stronger spin-orbit contact contribution (compare the values of $C_i^{\rho\nabla J}$ from Table IV). In Ref. [45] it was found that Skyrme functionals perform poorly on single-particle energies. The marked differences between SLy4' and N²LO single-particle spectra indicate that this situation may be improved.

However, as discussed in the previous section, all tensor contributions (contact term and finite-range contributions) have been set to zero to avoid the unnaturally large and strongly canceling values for $C_i^{\rho\nabla J}$ and $C_i^{J^2}$ that arise in the present

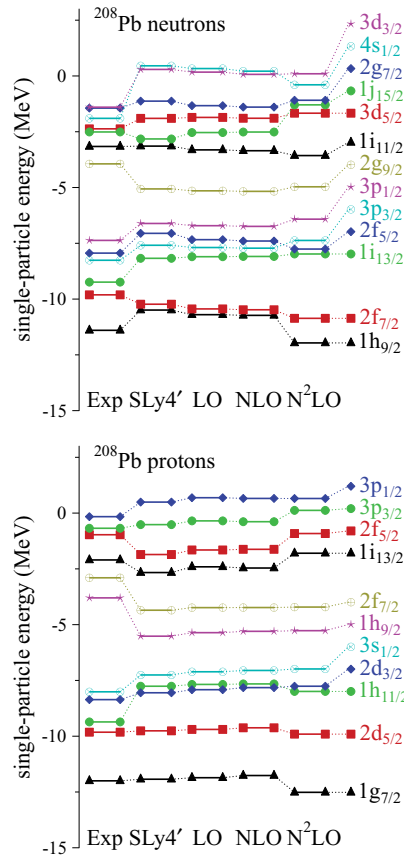


FIG. 3. (Color online) Comparison of ^{208}Pb experimental single-particle energies (in MeV) for neutrons and protons with canonical single-particle energies, calculated with the standard SLy4' functional and the LO, NLO, and N²LO DME functionals.

optimization protocol. Because the interplay between tensor and spin-orbit terms is crucial to understanding the evolution of nuclear shell structure, a detailed comparison of single-particle energies to data and standard Skyrme functionals is not appropriate with the present restricted optimization.

Similar comparisons between SLy4', LO, NLO, and N²LO results are shown in Fig. 4 for the two-neutron separation energies (top panel), neutron rms radii (middle panel), and the average neutron gaps (bottom panel) for nuclei in the Ni chain in the region up to the neutron drip line. Again, the comparison in Fig. 4 shows similar behaviors for the Skyrme- and DME-based functionals, with the largest deviations coming at N²LO. Let us remember, though, that small differences in separation energies can play an important role for reliable predictions of the position of the neutron drip line. As in the case of different Skyrme parametrizations, the DME functionals could lead to a shift in this prediction.

The fact that the Skyrme and DME functionals produce very similar results for this pool of observables is, in fact, encouraging, because we do not want to lose the good features that phenomenological functionals based on the Skyrme force have acquired over the years. However, it would also be disappointing if the rich, microscopically derived and nontrivial density dependence of the DME functionals could

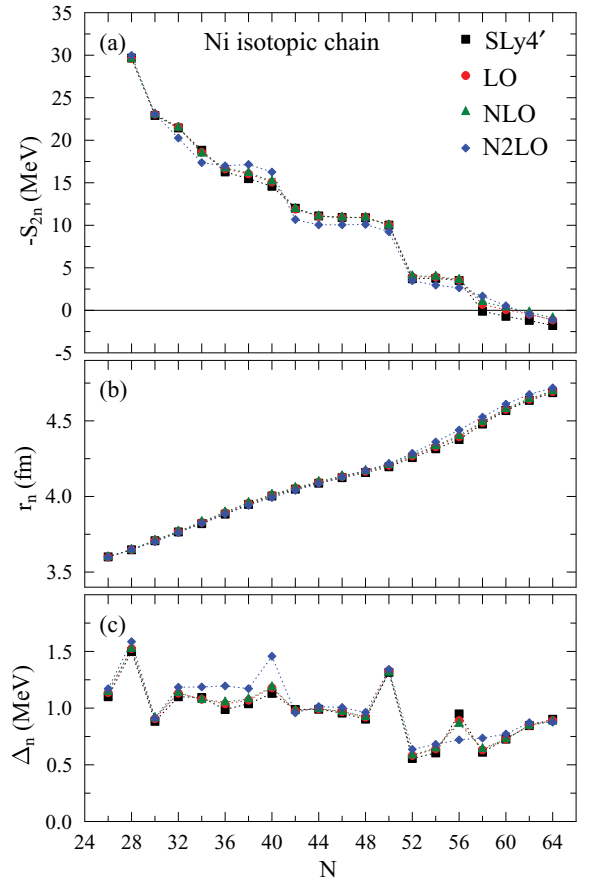


FIG. 4. (Color online) Two-neutron separation energies (a), neutron rms radii (b), and average neutron pairing gaps (c) for the Ni isotopic chain of nuclei in the region of the neutron drip line, calculated with the standard SLy4' functional and the LO, NLO, and N²LO DME-based functionals.

not bring in new physics that cannot be captured by Skyrme functionals.

In this respect, nuclear deformation is an excellent probe, as it reflects the competition between the bulk properties of the interaction and its single-particle content. Located right after the onset of deformation, the nucleus ^{100}Zr is characterized by the coexistence of three minima—oblate, spherical, and prolate—the relative position of which is highly sensitive to the interaction. Figure 5 shows that, in contrast to the Skyrme functional, the oblate and prolate minimum for DME functionals have almost the same energy (shape coexistence). At N²LO, the difference is even more marked, as the spherical minimum disappears and is shifted at small prolate deformation. This behavior of the DME functionals can probably be related to a combination of small differences in single-particle energies of closed-shell nuclei (see Fig. 3), as well as rather different surface bulk properties, see the value of coupling constants in Table IV. Indeed, it is a particularity of that new generation of EDF parametrizations to provide surface and spin-orbit terms with density-dependent couplings.

Another example of systematic differences is seen in the proton rms radii along the Ca isotopic chain as shown in Fig. 6.

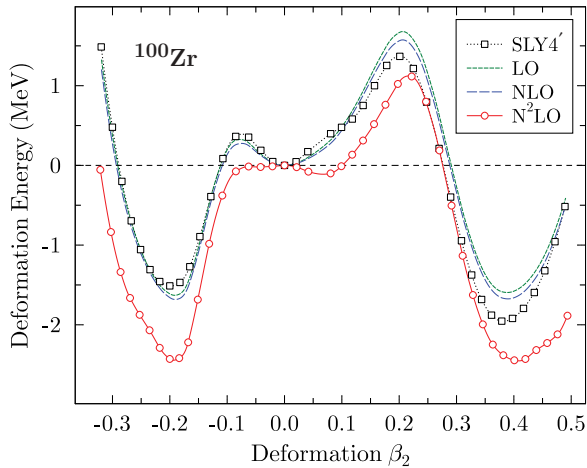


FIG. 5. (Color online) Deformation energy for the nucleus ^{100}Zr calculated with standard SLY4' functional (dotted line, squares) and the DME functional in LO (dashed line), NLO (long-dashed line), and N^2LO (solid line, circles).

Because r.m.s. radii were not included in the pre-optimization of the DME functional, the particular value of the proton radius is irrelevant. However, the isotopic trend is a marker for the isovector channels of the functional, and the differences of slopes between the Skyrme and DME functionals and the curvature between LO, NLO, and N^2LO might be indicative of new physics.

Whether these changes improve or deteriorate the quality of the current functional with respect to the experimental data is irrelevant, as the parametrization of Table IV should only be thought of as a prototype. A detailed study of the capabilities of DME functionals to reproduce experimental data, as well as more systematic comparison with standard parametrizations of the Skyrme functional, will be performed once a more

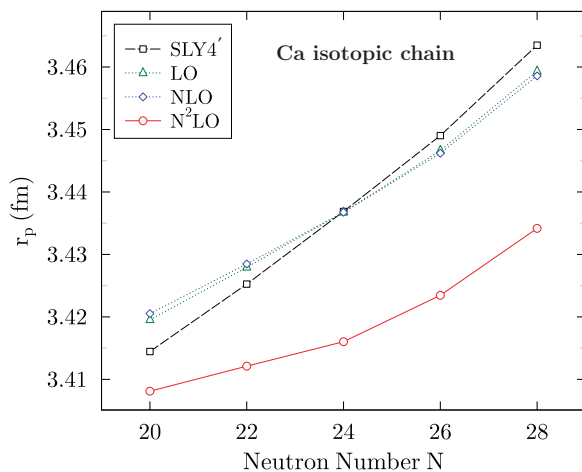


FIG. 6. (Color online) Comparison of the proton rms radii of nuclei along the Ca chain calculated with the standard SLY4' functional (long-dashed line with squares) and the DME functional in LO (dashed line with triangles), NLO (dashed line with diamonds), and N^2LO (solid line with circles).

comprehensive optimization procedure, such as the one used in Ref. [33], has been carried out.

VII. CONCLUSIONS

In the present article, we have given a practitioner's view of how the microscopically motivated DME functional of Gebremariam *et al.* [23], which possesses a much richer set of density dependencies than traditional Skyrme functionals, can be implemented in existing Skyrme HFB codes. Empirical INM properties are used to constrain the volume parameters of the Skyrme-like part, followed by a restricted SVD optimization procedure to fix its density-independent surface parameters. We find that the proposed functional gives numerically stable results and exhibits a small but systematic reduction in χ^2 compared to standard Skyrme functionals, thus justifying its suitability for future global optimizations and large-scale calculations.

The DME-based functional takes the same general form as standard Skyrme functionals, with the key difference that each coupling is composed of a density-independent Skyrme-like piece that is optimized to data, plus a density-dependent coupling function determined solely (no free parameters) from the HF contributions of the underlying finite-range NN and NNN interactions. In this way, the functional is split into a parameter-free "long-range" piece that is directly linked to underlying NN and NNN pion-exchange contributions (treated at the HF level) and a short-range piece that is identical in form to the standard Skyrme functional with parameters that are optimized to data.

After reviewing the structure of the DME-based functional and motivating the semiphenomenological approach used in the present work, it was demonstrated how the free contact parameters entering the volume part of the functional can be eliminated in a one-to-one fashion in terms of equilibrium INM characteristics. The influence of the finite-range DME contributions to symmetric and neutron INM was investigated with the most significant modification seen in the N^2LO case when the three-body interaction is taken into account. In this case, we find a reasonable incompressibility $K^{\text{NM}} = 230$ MeV with a Skyrme parameter $\gamma \sim 1$, a result that cannot be achieved within the standard Skyrme functional.

A preliminary (pre-) optimization procedure for surface and pairing parameters using the SVD-optimization algorithm was performed using the binding energies of 72 spherical and deformed nuclei, as well as 8 OEM differences. It was found that the pre-optimized DME-based functional performs as well or slightly better than the standard Skyrme functional with respect to the optimized binding energies and OEM differences. The same is true also for other nuclear characteristics, for example, nuclear rms radii, pairing gaps, separation energies, and single-particle energies, as well as for nuclei that are not included in the optimization. These preliminary results are very encouraging, as they imply that more elaborate global optimizations of the DME functional will, at the very worst, preserve the already impressive level of performance provided by traditional Skyrme functionals and very likely improve on them.

The present results have been obtained under two restrictions, which are not expected to modify our general conclusions and which will be removed in a future work. First, the NN Hartree contributions have been treated within the local density approximation. However, they can be easily taken into account exactly, as the computational cost is the same as for the calculation of the Coulomb direct term, which is already included in nuclear EDF calculations.

Much more important, insofar as it plays a central role in future investigations of the spectroscopic and single-particle properties of the new functional, is the neglect of the tensor contributions in the present study. The issue is that in the present optimization procedure, the contact tensor coupling constant cannot be released for optimization together with the spin-orbit coupling constant, as the optimization drives both couplings to unnaturally large (and strongly canceling) values. It should be noted that this difficulty is not specific to the DME-based functional, as similar issues arise with the standard Skyrme functional. The next step, removing both limitations mentioned earlier, is to apply a complete optimization procedure with the DME-based functional and perform systematic comparisons to the standard Skyrme functional and experimental data. Work in this direction is already in progress.

ACKNOWLEDGMENTS

We thank W. Nazarewicz, T. Papenbrock, and T. Lesinski for useful discussions. This work was supported by the Office of Nuclear Physics, US Department of Energy, under Contracts No. DE-FC02-09ER41583 (UNEDF SciDAC Collaboration), No. DE-FG02-96ER40963, No. DE-FC02-07ER41457, No. DE-FG02-07ER41529 (University of Tennessee), No. DE-FG0587ER40361 (Joint Institute for Heavy Ion Research), and No. DE-FC02-09ER41585 (Michigan State University) and the National Science Foundation under Grants No. PHY-0653312 and No. PHY-0758125. Computational resources were provided through an INCITE grant ‘‘Computational Nuclear Structure’’ by the National Center for Computational Sciences (NCCS) and the National Institute for Computational Sciences (NICS) at Oak Ridge National Laboratory.

APPENDIX A: DME SKELETON EXPRESSIONS

The lengthy analytic expressions for the DME couplings tend to obscure their underlying structural simplicity. Therefore, it is more illuminating to display the couplings in a ‘‘skeleton form’’ that still conveys its nontrivial density dependence.

The DME coupling $g_t^m(u)$ is given as a sum of LO, NLO, and N^2 LO contributions (recall $u = k_F/m_\pi$),

$$g_t^m(u) = g_t^m(u)|_{\text{LO}} + g_t^m(u)|_{\text{NLO}} + g_t^m(u)|_{\text{N}^2\text{LO}}, \quad (\text{A1})$$

where $t = 0, 1$ and the index m runs over the standard bilinear forms $\{\rho_t^2, \rho_t \tau_t, \rho_t \Delta \rho_t, \mathbf{J}_t^2, \mathbf{J}_t \nabla \rho_t\}$. These contributions are

of the following generic form:

$$g(u)|_{\text{LO}} = \alpha_0^g + \beta_0^g \log(1 + 4u^2) + \gamma_0^g \arctan(2u), \quad (\text{A2})$$

$$g(u)|_{\text{NLO}} = \alpha_1^g + \beta_1^g (\log(1 + 2u^2 + 2u\sqrt{1+u^2}))^2 + \gamma_1^g \sqrt{1+u^2} \log(1 + 2u^2 + 2u\sqrt{1+u^2}), \quad (\text{A3})$$

$$g(u)|_{\text{N}^2\text{LO}} = \alpha_2^g + \beta_2^g \log(1 + u^2) + \gamma_2 \arctan(u), \quad (\text{A4})$$

where $\alpha_k^g = \alpha_k^g(u)$, $\beta_k^g = \beta_k^g(u)$, and $\gamma_k^g = \gamma_k^g(u)$ are rational polynomials in u , with their dependence on t and m not explicitly shown. The explicit expressions for $k = 0, 1, 2$ are given in Ref. [23] and the companion MATHEMATICA notebooks.

In a similar way, the DME couplings $h_{tt'}^m(u)$ that collect the N^2 LO NNN contributions read

$$h_{tt'}^m(u) = \alpha_0^h + \beta_0^h \log(1 + 4u^2) + \beta_1^h [\log(1 + 4u^2)]^2 + \gamma_0^h \arctan(u) + \gamma_1^h [\arctan(2u)]^2 + \gamma_2^h \log(1 + 4u^2) \arctan(2u), \quad (\text{A5})$$

where the explicit expressions for the rational polynomials $\alpha_k^h = \alpha_k^h(u)$, $\beta_k^h = \beta_k^h(u)$, and $\gamma_k^h = \gamma_k^h(u)$, with their dependence on t and m , are not explicitly shown.

APPENDIX B: COUPLING CONSTANTS AND tx PARAMETRIZATION

Using the following explicit one-to-one relation between C_t^m parameters and the (t, x) Skyrme parameters,

$$C_0^{\rho_0 \rho_0} = \frac{3t_0}{8}, \quad C_0^{\rho_1 \rho_1} = -\frac{t_0}{4} \left(x_0 + \frac{1}{2} \right), \quad (\text{B1})$$

$$C_D^{\rho_0 \rho_0} = \frac{t_3}{16}, \quad C_D^{\rho_1 \rho_1} = -\frac{t_3}{24} \left(x_3 + \frac{1}{2} \right), \quad (\text{B2})$$

$$C^{\rho_0 \Delta \rho_0} = \frac{t_2}{16} \left(x_2 + \frac{5}{4} \right) - \frac{9}{64} t_1, \quad (\text{B3})$$

$$C^{\rho_1 \Delta \rho_1} = \frac{3t_1}{32} \left(x_1 + \frac{1}{2} \right) + \frac{t_2}{32} \left(x_2 + \frac{1}{2} \right), \quad (\text{B4})$$

$$C^{\rho_0 \tau_0} = \frac{3t_1}{16} + \frac{t_2}{4} \left(x_2 + \frac{5}{4} \right), \quad (\text{B5})$$

$$C^{\rho_1 \tau_1} = -\frac{t_1}{8} \left(x_1 + \frac{1}{2} \right) + \frac{t_2}{8} \left(x_2 + \frac{1}{2} \right), \quad (\text{B6})$$

$$C^{J_0^2} = -\frac{t_1}{16} \left(x_1 - \frac{1}{2} \right) - \frac{t_2}{16} \left(x_2 + \frac{1}{2} \right) + \frac{5}{32} (3t_0 + t_e), \quad (\text{B7})$$

$$C^{J_t^2} = \frac{1}{32} (t_1 - t_2) + \frac{5}{16} (t_0 - t_e), \quad (\text{B8})$$

$$C^{\rho_0 \nabla J_0} = -b_4 - \frac{1}{2} b_4', \quad C^{\rho_1 \nabla J_1} = -\frac{1}{2} b_4', \quad (\text{B9})$$

and substituting them into Eq. (23), one can verify that the contact part of the DME functional (23) is equivalent to the

well-known Skyrme energy density:

$$\begin{aligned}
\mathcal{H}^c(\mathbf{r}) = & \frac{\hbar^2}{2m} \tau + \frac{t_0}{2} \left[\left(\frac{x_0}{2} + 1 \right) \rho^2 - \left(x_0 + \frac{1}{2} \right) \sum_q \rho_q^2 \right] \\
& + \frac{t_1}{4} \left[\left(\frac{x_1}{2} + 1 \right) \rho \tau - \left(x_1 + \frac{1}{2} \right) \sum_q \rho_q \tau_q \right] \\
& + \frac{t_2}{4} \left[\left(\frac{x_2}{2} + 1 \right) \rho \tau + \left(x_2 + \frac{1}{2} \right) \sum_q \rho_q \tau_q \right] \\
& - \frac{3t_1}{16} \left[\left(\frac{x_1}{2} + 1 \right) \rho \Delta \rho + \left(x_1 + \frac{1}{2} \right) \sum_q \rho_q \Delta \rho_q \right] \\
& + \frac{t_2}{16} \left[\left(\frac{x_2}{2} + 1 \right) \rho \Delta \rho + \left(x_2 + \frac{1}{2} \right) \sum_q \rho_q \Delta \rho_q \right] \\
& + \frac{t_3}{12} \left[\left(\frac{x_3}{2} + 1 \right) \rho^2 - \left(x_3 + \frac{1}{2} \right) \sum_q \rho_q^2 \right] \rho^\gamma \\
& - \frac{1}{8} [t_1 x_1 + t_2 x_2 - 5(t_0 + t_e)] \sum_q J_q^2 \\
& - \frac{1}{16} \left[t_1 \left(x_1 - 1 \right) + t_2 \left(x_2 + 1 \right) - 10t_0 \right] \mathbf{J}_n \cdot \mathbf{J}_p \\
& - \left(b_4 \rho \nabla \cdot \mathbf{J} + b'_4 \sum_q \rho_q \nabla \cdot \mathbf{J}_q \right), \quad (\text{B10})
\end{aligned}$$

where in neutron-proton notation $q = (n, p)$, densities without an index stand for the total densities, for example, $\rho = \rho_n + \rho_p$, $\tau = \tau_n + \tau_p$, and $\mathbf{J} = \mathbf{J}_n + \mathbf{J}_p$.

APPENDIX C: DME FUNCTIONS FOR INM

The explicit expression for functions appearing in the INM equations are

$$\begin{aligned}
A_\gamma(u) = & (u g_0^{\prime\rho} + u^2 g_0^{\prime\rho\rho}) \rho_c + (9h_0^\rho + 7uh_0^{\prime\rho} + u^2 h_0^{\prime\rho\rho}) \rho_c^2 \\
& + (5u g_0^{\prime\rho\tau} + u^2 g_0^{\prime\rho\tau\tau}) \rho_c \tau_c \\
& + (21h_0^{\rho\tau} + 11uh_0^{\prime\rho\tau} + u^2 h_0^{\prime\rho\tau\tau}) \rho_c^2 \tau_c, \quad (\text{C1})
\end{aligned}$$

$$\begin{aligned}
B_\gamma(u) = & 3u g_0^{\prime\rho} \rho_c + (9h_0^\rho + 3uh_0^{\prime\rho}) \rho_c^2 \\
& + 3u g_0^{\prime\rho\tau} \rho_c \tau_c + (9h_0^{\rho\tau} + 3uh_0^{\prime\rho\tau}) \rho_c^2 \tau_c, \quad (\text{C2})
\end{aligned}$$

$$\begin{aligned}
A_{00}(u) = & (u g_0^{\prime\rho} - 3\gamma g_0^\rho) \rho_c + (uh_0^{\prime\rho} - 3(\gamma - 1)h_0^\rho) \rho_c^2 \\
& + u g_0^{\prime\rho\tau} \rho_c \tau_c + (3h_0^{\rho\tau} + uh_0^{\prime\rho\tau}) \rho_c^2 \tau_c, \quad (\text{C3})
\end{aligned}$$

$$\begin{aligned}
A_{0D}(u) = & -u g_0^{\prime\rho} \rho_c - (3h_0^\rho + uh_0^{\prime\rho}) \rho_c^2 \\
& - u g_0^{\prime\rho\tau} \rho_c \tau_c - (3h_0^{\rho\tau} + uh_0^{\prime\rho\tau}) \rho_c^2 \tau_c, \quad (\text{C4})
\end{aligned}$$

$$\begin{aligned}
A_{10}(u) = & 9(-3\gamma g_1^\rho + u g_1^{\prime\rho}) \rho_c + 9(3(1 - \gamma)h_1^\rho + uh_1^{\prime\rho}) \rho_c^2 \\
& + 5((8 - 12\gamma)g_0^{\rho\tau} + u(g_0^{\prime\rho\tau} + 3g_1^{\prime\rho\tau})) \rho_c \tau_c \\
& + (5(11 - 12\gamma)h_0^{\rho\tau} - 27\gamma h_{10}^{\rho\tau}) \rho_c^2 \tau_c \\
& + 45(h_{10}^{\rho\tau} + h_1^{\rho\tau}) \rho_c^2 \tau_c + u(5h_0^{\prime\rho\tau} + 9h_{10}^{\prime\rho\tau}) \rho_c^2 \tau_c \\
& + 15uh_1^{\prime\rho\tau} \rho_c^4 \tau_c^2, \quad (\text{C5})
\end{aligned}$$

$$\begin{aligned}
A_{1D}(u) = & -9u g_1^{\prime\rho} \rho_c - 9(3h_1^\rho + uh_1^{\prime\rho}) \rho_c^2 \\
& - 5(8g_0^{\rho\tau} + u g_0^{\prime\rho\tau} + 3u g_1^{\prime\rho\tau}) \rho_c \tau_c \\
& - 5(11h_0^{\rho\tau} + 9h_1^{\rho\tau} + 9h_{10}^{\rho\tau}) \rho_c^2 \tau_c \\
& - u(5h_0^{\prime\rho\tau} + 15h_1^{\prime\rho\tau} + 9h_{10}^{\prime\rho\tau}) \rho_c^2 \tau_c, \quad (\text{C6})
\end{aligned}$$

where prime and double prime denote the first and second derivative with respect of u , respectively.

-
- [1] S. C. Pieper, *Nucl. Phys. A* **751**, 516 (2005).
[2] S. Quaglioni and P. Navratil, *Few Body Syst.* **44**, 337 (2008).
[3] G. Hagen, T. Papenbrock, D. J. Dean, and M. Hjorth-Jensen, *Phys. Rev. Lett.* **101**, 092502 (2008).
[4] M. Bender, P.-H. Heenen, and P.-G. Reinhard, *Rev. Mod. Phys.* **75**, 121 (2003).
[5] G. F. Bertsch, D. J. Dean, and W. Nazarewicz, *SciDAC Rev.* **6**, 42 (2007).
[6] T. Lesinski, T. Duguet, K. Bennaceur, and J. Meyer, *Eur. Phys. J. A* **40**, 121 (2009).
[7] J. E. Drut, R. J. Furnstahl, and L. Platter, *Prog. Part. Nucl. Phys.* **64**, 120 (2010).
[8] T. Duguet and T. Lesinski, *AIP Conf. Proc.* **1165**, 243 (2009).
[9] S. K. Bogner, R. J. Furnstahl, and L. Platter, *Eur. Phys. J. A* **39**, 219 (2009).
[10] N. Kaiser, *Phys. Rev. C* **68**, 014323 (2003).
[11] N. Kaiser and W. Weise, *Nucl. Phys. A* **836**, 256 (2010).
[12] N. Kaiser, *Eur. Phys. J. A* **45**, 61 (2010).
[13] S. K. Bogner, A. Schwenk, R. J. Furnstahl, and A. Nogga, *Nucl. Phys. A* **763**, 59 (2005).
[14] S. K. Bogner, R. J. Furnstahl, S. Ramanan, and A. Schwenk, *Nucl. Phys. A* **784**, 79 (2007).
[15] S. K. Bogner, R. J. Furnstahl, and R. J. Perry, *Phys. Rev. C* **75**, 061001 (2007).
[16] S. K. Bogner, R. J. Furnstahl, A. Nogga, and A. Schwenk, [arXiv:0903.3366](https://arxiv.org/abs/0903.3366) [nucl-th].
[17] S. K. Bogner, R. J. Furnstahl, and A. Schwenk, *Prog. Part. Nucl. Phys.* **65**, 94 (2010).
[18] R. Roth, P. Papakonstantinou, N. Paar, H. Hergert, T. Neff, and H. Feldmeier, *Phys. Rev. C* **73**, 044312 (2006).
[19] R. Roth, S. Reinhardt, and H. Hergert, *Phys. Rev. C* **77**, 064003 (2008).
[20] J. Negele and D. Vautherin, *Phys. Rev. C* **5**, 1472 (1972).
[21] T. Lesinski, M. Bender, K. Bennaceur, T. Duguet, and J. Meyer, *Phys. Rev. C* **76**, 014312 (2007).
[22] B. Gebremariam, T. Duguet, and S. K. Bogner, *Phys. Rev. C* **82**, 014305 (2010).
[23] B. Gebremariam, S. K. Bogner, and T. Duguet, [arXiv:1003.5210](https://arxiv.org/abs/1003.5210) [nucl-th].
[24] B. Gebremariam, S. K. Bogner, and T. Duguet, *Comput. Phys. Commun.* **181**, 1167 (2010).
[25] X. Campi and A. Bouyssy, *Phys. Lett. B* **73**, 263 (1978).
[26] J. Negele and D. Vautherin, *Phys. Rev. C* **11**, 1031 (1975).
[27] F. Hofmann and H. Lenske, *Phys. Rev. C* **57**, 2281 (1998).
[28] N. Kaiser, S. Fritsch, and W. Weise, *Nucl. Phys. A* **724**, 47 (2003).
[29] M. Kortelainen and M. Stoitsov (to be published).
[30] H. W. Hammer and R. J. Furnstahl, *Nucl. Phys. A* **678**, 277 (2000).

- [31] E. Epelbaum, W. Glockle, and Ulf-G. Meissner, *Nucl. Phys. A* **747**, 362 (2005).
- [32] D. Sprung, M. Vallieres, X. Campi, and C.-M. Ko, *Nucl. Phys. A* **253**, 1 (1975).
- [33] M. Kortelainen *et al.*, *Phys. Rev. C* **82**, 024313 (2010).
- [34] E. Chabanat, P. Bonche, P. Haensel, J. Meyer, and R. Schaeffer, *Nucl. Phys. A* **635**, 231 (1998).
- [35] A. Akmal, V. R. Pandharipande, and D. G. Ravenhall, *Phys. Rev. C* **58**, 1804 (1998).
- [36] D. Vautherin and D. M. Brink, *Phys. Rev. C* **5**, 626 (1972).
- [37] R. M. Koehl, G. K. Odom, and G. Scuseria, *Mol. Phys.* **87**, 835 (1995).
- [38] M. Kortelainen and T. Lesinski, *J. Phys. G* **37**, 064039 (2010).
- [39] G. F. Bertsch, B. Sabbey, and M. Uusnaki, *Phys. Rev. C* **71**, 054311 (2005).
- [40] J. Toivanen, J. Dobaczewski, M. Kortelainen, and K. Mizuyama, *Phys. Rev. C* **78**, 034306 (2008).
- [41] J. Dobaczewski, W. Nazarewicz, and M. Stoitsov, in *The Nuclear Many-Body Problem 2001*, edited by W. Nazarewicz and D. Vretenar (Kluwer Academic, Dordrecht, 2002), p. 181.
- [42] M. V. Stoitsov, J. Dobaczewski, W. Nazarewicz, and P. Ring, *Comput. Phys. Commun.* **167**, 43 (2005).
- [43] M. V. Stoitsov, J. Dobaczewski, R. Kirchner, W. Nazarewicz, and J. Terasaki, *Phys. Rev. C* **76**, 014308 (2007).
- [44] N. Schwierz, I. Wiedenhover, and A. Volya, [arXiv:0709.3525](https://arxiv.org/abs/0709.3525) [nucl-th].
- [45] M. Kortelainen, J. Dobaczewski, K. Mizuyama, and J. Toivanen, *Phys. Rev. C* **77**, 064307 (2008).